Composites Part B 253 (2023) 110529

Contents lists available at ScienceDirect

Composites Part B

journal homepage: www.elsevier.com/locate/composites

Benchmark test for mode I fatigue-driven delamination in GFRP composite laminates: Experimental results and simulation with the inter-laminar damage model implemented in SAMCEF

L. Carreras [a,b,*], B.L.V. Bak [a], S.M. Jensen [a], C. Lequesne [c], H. Xiong [c], E. Lindgaard [a]

[a] CraCS Research Group (cracs.aau.dk), Department of Materials and Production, Aalborg University, Fibigerstraede 16, DK-9220 Aalborg East, Denmark
[b] AMADE Research Group, Polytechnic School, University of Girona, Campus Montilivi s/n, E-17003 Girona, Spain
[c] Siemens Digital Industries Software, Rue des Chasseurs Ardennais 8, BE-4031 Angleur, Belgium

ARTICLE INFO

Keywords:
GFRP laminates
Delamination
Fatigue
Cohesive zone model
Finite element method

ABSTRACT

Adopting effective and accurate numerical tools capable of predicting damage effects on the structure reduces design, certification, and maintenance costs. However, the tools to assess progressive delamination under high-cycle fatigue are rarely validated against realistic benchmark tests different from simple tests on coupon specimens that can be simplified to a 2D geometry. This work presents a benchmark test on a demonstrator specimen made of a non-crimp fabric laminated Glass Fiber Reinforced Polymer (GFRP) used in the wind energy industry. The case shows varying crack growth rates and crack front shape over the fatigue life, making it more representative of structures in service than coupon specimens. Moreover, the test is simulated with the first commercially available tool to assess progressive delamination under high-cycle fatigue loading based on a cohesive zone model approach. The method is implemented in the Simcenter Samcef 2021.2 software package dedicated to mechanical virtual prototyping. A characterization testing campaign on coupon specimens is carried out to obtain the material properties for the method. The numerical method can reproduce the experimental results on the demonstrator specimen regarding crack front shape evolution and crack front location versus the number of fatigue cycles.

1. Introduction

One of the most critical damage mechanisms in laminated composite structures is fatigue-driven delamination since it can be difficult to detect, and it may greatly compromise the structural integrity. There are two alternatives to deal with fatigue-driven delamination in the design of composite structures [1]: (1) the non-growth criterion, which inevitably leads to conservative designs, and (2) the damage tolerance approach, which allows crack growth provided that it does not reach an unsafe size during service. The latter leads to more efficient design, but safety must be guaranteed. Thus, fatigue failure prediction is crucial for accurately assessing the service life and as a planning tool for maintenance actions.

The main reason that hinders the prediction of the mechanical response of laminated composite structures is the failure process, which consists of different complex damage mechanisms. Various engineering industries, such as aeronautical, wind energy and automotive take advantage of the wide range of finite element method (FEM) simulation options to aid the design process, and maintenance protocols of their products. Some structural analysis FEM codes can predict the occurrence of different damage mechanisms. Usually, cohesive zone models (CZM) [2–12] are employed for describing inter-laminar damage, also called delamination. Although several commercial FEM packages include specific components for the simulation of delamination under quasi-static loading, none of them allow for simulation of fatigue driven-delamination. Thus, there is a need for efficient and reliable technologies that are made available to mechanical engineering professionals to account for delamination in complex, layered composite structures under fatigue loading.

With the exception of the fatigue growth criterion using the direct cyclic approach available in Abaqus/standard [13], simulation of fatigue-driven delamination is limited to in-house research codes. Multiple CZMs exist in the scientific literature that deal with fatigue-driven delamination [14–25]. However, most of them are limited to two-dimensional (2D) applications or they have not been fully validated in three-dimensional (3D) problems. This means that they are not applicable or have not been validated for predicting crack front evolution

* Corresponding author at: AMADE Research Group, Polytechnic School, University of Girona, Campus Montilivi s/n, E-17003 Girona, Spain.
E-mail addresses: laura.carreras@udg.edu (L. Carreras), brianbak@mp.aau.dk (B.L.V. Bak), smj@mp.aau.dk (S.M. Jensen), cedric.lequesne@siemens.com (C. Lequesne), hu.xiong@siemens.com (H. Xiong), elo@mp.aau.dk (E. Lindgaard).

https://doi.org/10.1016/j.compositesb.2023.110529
Received 30 August 2022; Received in revised form 9 December 2022; Accepted 11 January 2023
Available online 25 January 2023

with varying geometry over the fatigue life, as it is likely to occur in composite structures in service.

One exception is the method presented by Carreras et al. [26]. The method was implemented as a user-defined cohesive element in Abaqus, and the predicting capabilities of this method were demonstrated by comparison with experimental benchmark tests on carbon fibre reinforced polymer (CFRP) specimens [27]. The model was shown to be the best at reproducing the crack growth rate and total crack growth in a 2D benchmark study [28], where six different computational methods for simulating fatigue-driven delamination based on a cohesive zone model approach and aimed at high-cycle fatigue were compared. The simulation results matched the experimental crack growth rate curve under different mode mixities and load ratios. Moreover, the simulation method was evaluated against a benchmark case loaded under cyclic displacement-control with varying crack front shape. In all cases, the simulation results matched the experimental data very well. All the input parameters introduced in the simulations presented in [26] were obtained experimentally from fatigue propagation tests on coupon specimens, thus avoiding calibrating the method to adjust any kind of fitting parameter. This, together with the demonstrated accuracy in predicting the delamination front evolution, make the method the perfect candidate to be integrated into the libraries of commercial FE codes as a built-in simulation function.

This paper presents a benchmark test on a demonstrator specimen made of a Glass Fibre Reinforced Polymer (GFRP) material system commercially applied in the wind turbine industry. Likewise the study carried out in [27], a wide DCB-like specimen with partially reinforced arms was used. A reinforcement in the middle of the width triggered the delamination front to change shape and propagation rate during the test. Thus, this work provides a new set of experimental data with a rich phenomenology of crack advance, while being geometrically simple enough to be simulated. Compared to the study shown in [27], the present benchmark experimental test was carried out on a different material system, a scaling on the specimen's dimensions and different boundary conditions. In addition, the data acquisition techniques and data reduction methods, both from the characterization tests and the validation tests, were different. In this case, the specimen was loaded in fatigue under pure moments using the test fixture developed in [29,30]. The bending moments applied to each arm were equal in magnitude and had opposite signs resulting in pure mode I crack opening. Taking advantage of the translucency of GFRP, the crack front location and shape during propagation was assessed using an automated digital image-based tracking method presented in [31] and further refined in [32].

Moreover, this paper describes the implementation of the simulation method for fatigue-driven delamination presented in [26] into the commercial finite element software Simcenter Samcef software package version 2021.2 [33]. Additional validation of the method against the presented benchmark test was done. Comparisons of the crack front location and shape from numerical and experimental results were made at certain cycles during the fatigue analysis.

The paper is structured as follows. In Section 2, the main theoretical concepts related to the 3D progressive delamination method [26] are presented. In Section 3.1, the methodology to characterize the input mode I interface properties is provided. In Section 3.2, the methodology followed to test the demonstrator specimen that will validate the model is described. In Section 4.1, the details of the implementation of the method in the Simcenter Samcef 2021.2 software are given. The procedure followed to carry out the simulation of the demonstrator specimen is explained in Section 4.2. In Sections 5.1 and 5.2, the results from the quasi-static and fatigue characterization testing campaigns are reported. In Section 5.3, the experimental and simulation results of the demonstrator benchmark case are compared. In Section 6, the computational efficiency of the intrinsic fatigue method implementation in Samcef is compared to the previous extrinsic Abaqus user-element implementation. Finally, in Section 7, a summary of the main achievements, impact and conclusions of this work are highlighted.

2. Cohesive zone model for 3D simulation of fatigue-driven delamination

The fatigue CZM was developed in four main steps, each one presented in different publications listed in the following.

- The kinematics of the cohesive element, as well as the constitutive model for static loading under mixed-mode conditions and its discretization into finite elements, were presented by Turon et al. [34,35].
- The point of departure for the fatigue damage rate formulation was the 2D simulation method for high-cycle fatigue-driven delamination developed by Bak et al. [20].
- The extension of the fatigue method for its application to 3D simulation required: (a) the development of a model for predicting the growth direction of a crack and (b) a method for calculating the J-integral on the cohesive interface.

  (a) An algorithm to determine the direction of crack propagation in delamination fronts modelled using a CZM approach was developed by Carreras et al. in [36].

  (b) A J-integral formulation applicable to cohesive interfaces for determining the mode-decomposed energy release rates in 3D simulations was presented by Carreras et al. in [37].
- Finally, all the aforementioned ingredients were combined in the 3D delamination simulation method for non-negligible fracture process zones and arbitrarily shaped crack fronts, presented by Carreras et al. in [26] and implemented in a user-defined cohesive element in Abaqus [13].

Moreover, the implementation in the Simcenter Samcef 2021.2 software, which will be presented in this paper, incorporates new features that enhanced the efficiency, usability and convergence capabilities for its application in an industrial and commercial environment. The specific functions to the built-in simulation tool available in the Simcenter Samcef 2021.2 software are described in Section 4.1.

The main concepts of the simulation method for fatigue-driven delamination presented in publications [20,26,34–37] are described as follows. The interfacial constitutive behaviour is formulated in terms of the separation, δ_i, between the two initially coincident surfaces bounding the plies and the associated cohesive traction, τ_i, that acts to tie the surfaces together. In the FE implementation, the cohesive behaviour is embedded into the mid-surface between the upper and the lower crack surfaces. The cohesive variables are decomposed into a mode I component (following the normal 3-direction to the mid-surface) and two shear components (following the tangential 1- and 2-directions to the mid-surface). An equivalent one-dimensional mixed-mode cohesive law is formulated in terms of the displacement jump norm, λ, and an equivalent one-dimensional traction, $\mu = f(\lambda)$, to address the process of fracture under varying mode-mixity. The CZM is formulated in the framework of damage mechanics to ensure irreversible crack propagation. The degradation process of the cohesive properties starts once the onset criterion is fulfilled, (λ_o, μ_o), and ends when the propagation criterion is reached, (λ_c, μ_c) with $\mu_c = 0$. The evolution of the damage variable associated with quasi-static loading is governed by the equivalent one-dimensional cohesive law and the kinematics of the cohesive element. An energy-based damage variable, D^e, is used and it is uniquely related to the stiffness-degrading damage variable D^K. D^e is defined as the ratio of specific dissipated energy due to fracture, ω_d, and the fracture toughness, $\mathcal{G}_c$ during degradation ($\lambda_o < \lambda_D < \lambda_c$). D^e exhibits linear dependency with the mixed-mode displacement jump associated with a given damage state, λ_D. An additional damage evolution due to cyclic loading is linked to a Paris' law-like description of the fatigue crack growth rate, $\mathrm{d}a/\mathrm{d}N = f(\mathcal{G})$. Following an envelope load approach for fatigue loading, the number of cycles is discretized and the damage variable is updated at each equilibrium step. The damage at a given number of cycles is

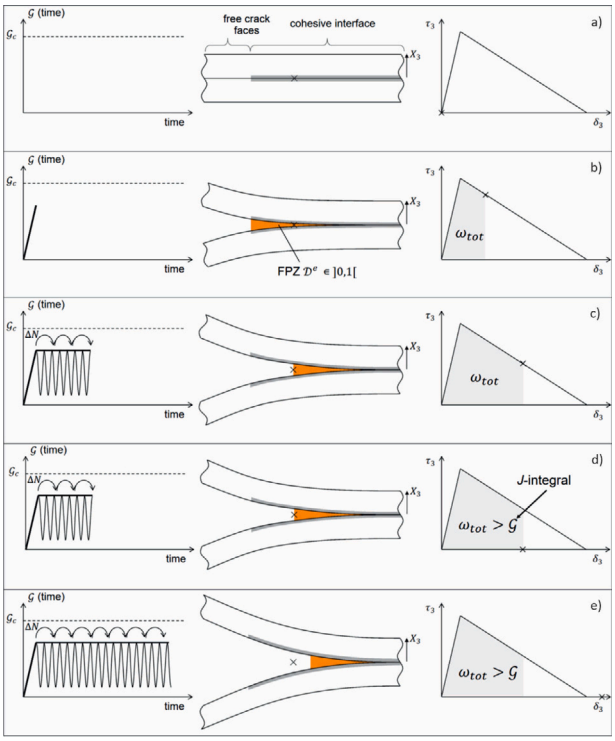

Fig. 1. Schematic example of a crack loaded in pure mode I fatigue. The distribution of traction and the displacement jump within the fracture process zone follows the quasi-static cohesive law until the condition for full damage is fulfilled (adapted from [20]). Note that for pure mode I crack opening $\lambda = \delta_3$ and $\mu = \tau_3$.

determined by integrating the damage rate, $\mathrm{d}D^e/\mathrm{d}N$. The maximum cyclic energy release rate, $\mathcal{G}$, is measured at each integration point using a 3D J-integral formulation expressed in a local crack coordinate system, x_i. The integration domain is reduced to a path contained in the delamination interface that follows the direction of crack propagation as determined by the growth driving direction (GDD), i.e. the direction where the total work in the cohesive interface (ω_{tot}) is performed at the highest rate relative to $\mathcal{G}_c$.

Fig. 1 exemplifies that the $\mu(\lambda)$ relation defined by the quasi-static model is maintained during fatigue-driven crack growth. In Fig. 1.(a), the unloaded and undamaged cohesive interface is shown. In Fig. 1.(b), the load is increased during the quasi-static ramping phase, and the point marked with a cross is contained in the fracture process zone (FPZ). In Fig. 1.(c), the crack has now propagated in the fatigue phase. In Fig. 1.(d), the value of the total specific work, ω_{tot}, at the point marked with a cross is then equal to or larger than the maximum cyclic energy release rate, $\mathcal{G}$, evaluated by means of the 3D J-integral. In order to apply the condition that the distributions of tractions and the displacement jumps within the fracture process zone are unchanged in the shift between quasi-static loading and fatigue loading, the traction drops to zero at the opening traction–displacement relation where $\omega_{tot} \geq \mathcal{G}$. In Fig. 1.(e), the fatigue phase is still running, but the point marked with a cross is fully damaged and hence not able to withstand any traction.

The implementation of the described CZM is summarized in the algorithm presented in Table A.7. Being N_n the number of cycles at the end of the last converged cycle increment, the inputs to the CZM are: The historical cycle jump, $\Delta N|_{Nn}$, the historical crack growth rate, $\mathrm{d}a/\mathrm{d}N|_{Nn}$, the displacement jumps, $\{\boldsymbol{\delta}\} = \{\delta_1, \delta_2, \delta_3\}^T$, the historical energy-based damage threshold variable, $D^e|_{Nn}$, and the material properties. In turn, the cohesive tractions, $\{\boldsymbol{\tau}\} = \{\tau_1, \tau_2, \tau_3\}^T$, the updated energy-based damage threshold variable, D^e, the constitutive tangent stiffness, $[\boldsymbol{C}_{\boldsymbol{\tau}}]$, the updated cycle jump, ΔN, and the updated crack growth rate, $\mathrm{d}a/\mathrm{d}N$ are the outputs of the CZM. The required material parameters are: (i) mode I and mode II onset displacement jumps, δ_{Io} and δ_{IIo}, related to the cohesive strengths, τ_{Io} and τ_{IIo}, (ii) mode I and mode II critical displacement jumps, δ_{Ic} and δ_{IIc}, related to the fracture toughness, $\mathcal{G}_{Ic}$ and $\mathcal{G}_{IIc}$, (iii) the Benzeggagh and Kenane exponent for the mixed-mode interpolation of the quasi-static properties, η, (iv) the mode I and mode II exponents and coefficients of the Paris' law-based expression for the crack growth rate, p_I, p_{II}, A_I and A_{II}, (v) the mixed-mode interpolation parameters for the fatigue properties, p_m and A_m, (vi) the mode I and mode II fatigue thresholds, $\mathcal{G}_{Ith}$ and $\mathcal{G}_{IIth}$ and (vii) the Benzeggagh and Kenane exponent for the mixed-mode interpolation of the fatigue threshold values, η_2. Finally, (viii) K is the initial effective stiffness, (ix) R is the load ratio and (x) Δa_t is a target for the maximum increment in crack length per solution sub-step.

Table 1
Dimensions (in mm) of the DCB coupon specimens quasi-statically tested for measuring the mode I fracture toughness, $\mathcal{G}_{Ic}$.

Specimen id	Thickness (micromet. ± 0.01)	Width (calliper ± 0.1)
C 01	12.15	27.8
C 02	12.30	27.8
C 03	12.15	27.8
C 04	12.10	27.6
C 05	12.18	28.1
C 06	12.22	27.8

Table 2
Dimensions (in mm) of the DCB coupon specimens tested for measuring the mode I fatigue properties, (A_I, p_I).

Specimen id	Thickness (micromet. ± 0.01)	Width (calliper ± 0.1)
E 01	12.18	27.8
E 04	12.27	27.7
F 11	12.20	27.5
F 16	12.00	28.0
F 17	12.28	27.7

3. Experimental testing

3.1. Characterization of material properties

The capability of the presented method to accurately predict delamination growth in problems that cannot be simplified to 2D models is assessed with a benchmark case that exhibits changes in crack front shape and growth rate as the crack propagates during the test. All the specimens used in this study were manufactured (stacked, cured and cut) by the company Siemens Gamesa Renewable Energy (SGRE). Specimens were made of a glass fibre reinforced epoxy composite material with a unidirectional (UD1340) architecture based on non-crimp fabrics with backing fibres in the ±45° directions (Biax100). The weight percentage of backing in the fibre was 7% and the area weight was 1.483 kg/m^2. A symmetrical stacking sequence of 12 plies was used with a 0°-0° interface at the midplane.

Measurements of the specimen thickness and width were taken at the midpoint and approximately 25 mm from either end. The average width and thickness of the specimens tested under quasi-static and fatigue loading are listed in Tables 1 and 2, respectively. All specimens were 700 mm long, and the initial crack length from the tab was 75 mm.

The elastic properties of the ply were provided by SGRE and are listed in Table 3. For the inter-laminar fracture properties, a characterization campaign was carried out to obtain the required material properties for the method presented in Section 2. Double cantilever beam (DCB) specimens made of 12 plies with a symmetric lay-up were used.

Three-point bending tests were performed to the seven specimens listed in Table 4 to obtain the flexural modulus, (E in Eq. (2)) used to calculate the energy release rate for the data reduction of the characterization tests.

Table 3
Laminate elastic properties of the validation material.

Laminate properties		
E_{11}	47.96	GPa
E_{22}	15.08	GPa
E_{33}	14.20	GPa
G_{12}	4.83	GPa
G_{13}	2.2	GPa
G_{23}	1.5	GPa
ν_{12}	0.308	–
ν_{13}	0.251	–
ν_{23}	0.335	–

Table 4
Flexural modulus obtained from three-point bending tests.

Specimen id	Flexural modulus, E_{11}^f (MPa)
F 11	37 846.94
E 04	35 496.33
F 08	36 265.31
E 03	37 908.46
E 01	37 870.40
F 16	38 947.61
F 17	36 093.39
Average	**37 204.06**

3.1.1. Mode I inter-laminar quasi-static properties

For quasi-static delamination testing of DCB specimens, the text fixture presented in [29] and later extended to fatigue loading in [30] was used (see Fig. 2). The text fixture produces pure bending moments on the arms of the DCB specimens using tensile loading input from the electro-mechanical testing machine (Zwick 100 kN). The concept of the test fixture is based on the principle from [38], and similar test fixtures have been applied for quasi-static testing in [29,39–41] and for fatigue testing in [30,42] of FRP laminates. The loading rig principle was redesigned in [29,30] to minimize unwanted effects from large displacements and rotations, thus allowing testing of more compliant specimens. A brief description of the basic loading principle of the applied test rig is given here and in Fig. 2. For further details, the reader is referred to [29,30]. Two moment-loading arms are attached to the DCB specimen to introduce pure bending moments. There is a wire-and-roller system that applies a force couple to each moment-loading arm. The system uses a single continuous wire, thus ensuring a constant wire traction force. This results in vertical, equal and opposite forces of magnitude $F/2$ that act transversely on the moment-loading arms. The resulting pure bending moment is given by:

$$M = \frac{F}{2}s \tag{1}$$

where F is the force measured at the load cell and s is the horizontal distance between the two points of load application (taking into account the wire-and-roller arrangement). In order to calculate the distance s, the angle of each moment-loading arm is measured continuously during testing using two inclinometers. The test fixture is capable of pure mode I and mixed mode I/II crack opening in quasi-static loading and pure mode I crack opening in fatigue loading. The mode I energy release rate, $\mathcal{G}$, can be determined based on the J-integral approach [39,43,44] and assuming plane strain conditions:

$$\mathcal{G} = 12(1-\nu_{13}\nu_{31})\frac{M^2}{E_{11}^f h^3 b^2} \tag{2}$$

where h is the height of each beam, b is the width of the DCB specimen, E_{11}^f is the flexural modulus, ν_{13} and ν_{31} are the major and minor Poisson's ratios (in this case, $\nu_{31} = \nu_{13}$), and M is the applied moment on each arm of the DCB specimen.

A batch of six DCB coupon specimens were tested. A pre-rotation of −7.5° and 7.5 was set at the upper and lower moment-loading arms, respectively, to compensate for the moment-loading arms rotation at the end of the test. The horizontal distance between the two points of load application, s, at the unloaded configuration was 167 mm. The average flexural modulus $E_{11}^f = 37\,204.06$ MPa, from Table 4, was used in Eq. (2) for calculating the energy release rate, $\mathcal{G}$.

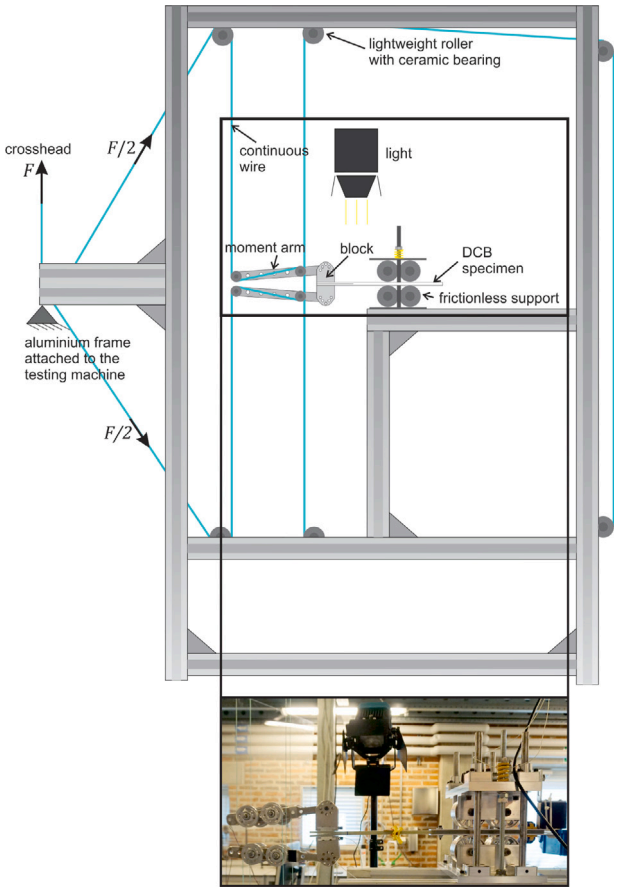

Fig. 2. Overview of test fixture for bending test of DCB specimen with bending moments.

3.1.2. Mode I inter-laminar fatigue properties

Fatigue testing was aimed at obtaining the crack growth rate curve, which relates the rate of crack propagation in mm/cycle with a Paris' law-based function of the maximum cyclic energy release rate (see Eq. (A.23)). Tests were run sinusoidally at constant-amplitude displacement with a load ratio, R, of 0.1 and a frequency of 5 Hz. A more compact pure mode I moment test fixture [42] than the one used for quasi-static testing (see Section 3.1.1) was used. The design was adapted to an electro-mechanical testing machine for static and fatigue testing (Instron Electropuls 10kN). A system of pulleys and wires was used to apply a bending moment to each DCB arm, as shown schematically in Fig. 3. In contrast to the previous testing rig, this set-up uses four separate wires. A prescribed displacement at the crosshead results in a reaction force, F, applied to each pulley at point A in Fig. 3. The reaction force, F, is measured at the load cell. The resulting traction in each vertical wire segment looped around the pulleys is $F/2$, as illustrated in the figure. Therefore, at points B and C, equal and opposite forces of magnitude $F/2$ act transversely on the DCB arm that result in a pure mode I bending moment given by Eq. (1), where s is the horizontal distance between points B and C as illustrated in Fig. 3. A support structure was installed to ensure that the longitudinal centre axis of the specimen remains horizontal as the prescribed sinusoidal displacement is applied.

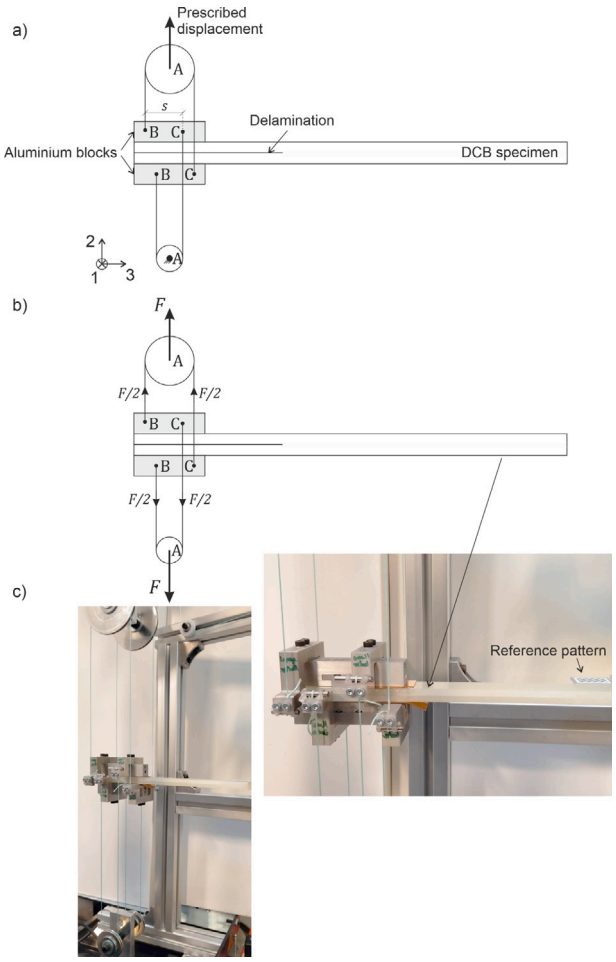

Fig. 3. Overview of the compact test fixture for bending test of DCB specimen with bending moments. (a) Kinematic conditions, (b) free body diagram with reaction forces and (c) picture of the test set up.

An automated digital image-based tracking method [31,32] was used to track the crack front position during the fatigue test (see Fig. 4). This method exploits the increased intensity of diffuse reflected light of the irregular surface of the newly formed crack area to highlight the location of the crack front. The crack tip at a certain number of loading cycles was taken as the averaged crack length across the specimen width. A PointGrey Blackfly (monocolour 2448 × 2048 pixels ethernet camera) with an Edmund optics 75 mm double Gauss lens was filming the top of the specimen, and two NILA ZAILA lights were applied on the same side of the specimen as the camera location. The lights were angled such that the light was reaching the specimen at an angle of approximately 45°. Changes in both the relative position and orientation of the camera and/or specimen were compensated by using a reference pattern attached to the specimen. The reference pattern was flat and placed such that it was coplanar with the top surface of the undamaged part of the specimen. The camera was synchronized with the tensile testing machine, and the images were acquired at intervals of 10 fatigue load cycles.

The images were used to determine the averaged crack length across the specimen width with respect to the number of cycles. The crack growth rate da/dN was determined by fitting a linear function to all data points within a moving fitting window of 1000 cycles × 2 mm centred around the point of interest [31]. The maximum cyclic energy release rate, $\mathcal{G}$, was calculated using Eq. (2).

A batch of five DCB coupon specimens were tested. Prior to the first fatigue cycle, the DCB specimens were quasi-statically loaded for at least 30 mm of crack extension. In this case, the corresponding flexural modulus for each specimen, listed in Table 4, was used in Eq. (2) for the calculation of the energy release rate. It was chosen to fit a Paris' law-based crack growth rate model to the combined data set and not to each specimen dataset since the differences between the datasets were up to 1 decade. This model was fitted to the combined data using a weighted linear least squares criterion on a linearized version of the original power law given by:

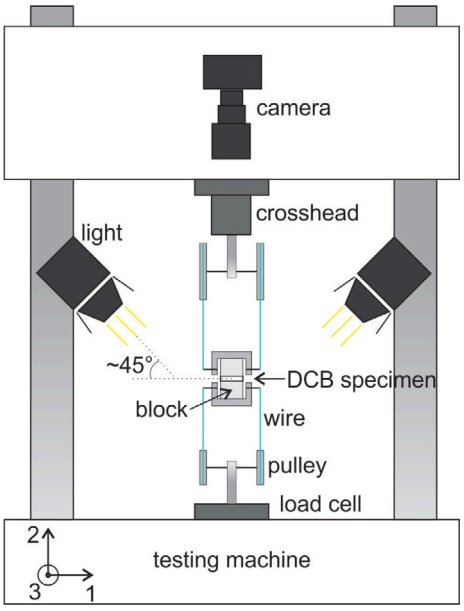

Fig. 4. Layout of the test setup with digital image acquisition to track the delamination front.

$$\log\left(\frac{da}{dN}\right) = \log\left(A_I\right) + p_I \log\left(\mathcal{G}\right) \tag{3}$$

It is worth noting that the data sets were not showing a log-linear trend for the entire $\mathcal{G}$ range explored during the fatigue tests. Thus, the fitting of a Paris' law-like expression did not match the dataset for the entire $\mathcal{G}$ range. In order to overcome this situation, the data sets were cropped to the applied $\mathcal{G}$ range in the demonstrator tests presented in Section 5.3. The crack growth rate da/dN was used as weight. The weighted least squares fit was obtained by minimizing the following expression with $\log(A_I)$ and p_I as the parameters to be determined.

$$\sum_{i=1}^{n}\left(\frac{da}{dN}\right)_i\left(\log\left(\frac{da}{dN}\right)_i - \log\left(A_I\right) + p_I \log\left(\mathcal{G}\right)_i\right)^2 \tag{4}$$

The spacing between data points in terms of $\mathcal{G}$ varied throughout the test in the sense that the spacing was large for high values of $\mathcal{G}$ and vice versa. Each dataset was linearly interpolated with evenly spaced energy release rate values before the fit was done in order not to let the spacing between data points bias the fit of the crack growth rate model in an uncontrolled manner. The same values of $\mathcal{G}$ were used for the interpolated values for all the datasets. The increment in $\mathcal{G}$ for the interpolated datasets was set to 0.1 J/m^2.

It is worth to mention that the Paris' law data obtained from characterization tests on coupon specimens depends on the amount of fibre bridging, as demonstrated in [45–49]. Thus, special care should be taken in material systems that develop a large fibre bridging zone. Since the method does not consider transient effects from the development of the fibre-bridging, it could provide non-conservative predictions.

3.2. Testing of the demonstrator specimens

The test specimens were made of a plate and two reinforcements made of the GFRP material system described in Section 3.1. The plate

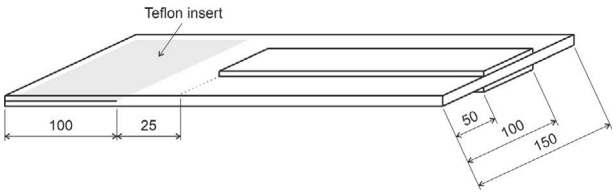

Fig. 5. Arrangement of the partially reinforced DCB specimen (units in mm).

Table 5
Load sequence of the fatigue tests performed on the demonstrator specimens.

Specimen id	Number of fatigue load steps	Applied maximum cyclic moment (N m)	Number of cycles of the fatigue load step
DEM_02	1	50	329,464
DEM_03	2	40 60	475,356 202,533
DEM_04	2	40 60	475,585 251,663

was made of eight plies oriented at 0°, was 700 mm long, 150 mm wide and had a 100 mm long initial straight pre-crack made by a Teflon insert at the mid-plane, as illustrated in Fig. 5. The two reinforcements were made of four plies of the same material and orientation, were 550 mm long and 50 mm wide, and were bonded on top and bottom sides of the specimen in order to promote curved delamination front.

The different elements (plate and reinforcements) of the demonstrator specimen were manufactured (stacked, cured and cut) by SGRE. The reinforcements were bonded to the plate at the AAU testing lab using the 2-component epoxy adhesive Permalock EP 708. A vacuum bag was used to ensure an even distribution of the adhesive through the entire plate-reinforcement interface. First, the adhesive was manually applied on both adherents with a two component cartridge gun. This makes sure that there was enough adhesive to cover the entire surfaces. Then, the reinforcement was put in place and aligned with guiding pins in the plate and reinforcement. The whole specimen was then introduced into a vacuum bag, with the outlet positioned near the reinforcement edge closest to the initial delamination. This was done to ensure enough adhesive at the edge, where the abrupt change in stiffness supplied by the reinforcement causes stress concentration at the bond interface.

Fatigue tests on the demonstrator specimens were done using the test fixture for delamination test of DCB specimens with pure bending moments presented in Section 3.1.1 and illustrated in Fig. 2. The applied bending moment is measured using strain gauges attached to the metal moment-loading arms on the test fixture. This provides direct measurements of the applied bending moment at the arms of the partially reinforced DCB specimen and the strain gauge measurements are used to control the fatigue tests. The same procedure has recently been applied in [30] to conduct moment-controlled cyclic tests. Tests were run sinusoidally at constant-amplitude moment with $R = 0.1$ and a frequency of 2 Hz.

A batch of three demonstrator specimens was tested. The load sequence in terms of applied moment and number of fatigue cycles is listed in Table 5 for every test specimen. The first test consisted of one single load step, meaning that the maximum cyclic applied moment was constant during the entire test. Due to the stiffening effect of the reinforcement, the crack propagation arrested at the reinforcement edge. In order to overcome the crack arrest, the two last tests consisted of two fatigue load steps (i.e. the applied maximum cyclic moment was increased to a higher level after a certain number of cycles). The increase of the load level during the second step promotes further crack propagation beyond the reinforcement edge.

A servo-hydraulic testing machine (Schenck 100 kN) was used. The combined experimental set-up used for the testing of the demonstrator specimen consisted of three computers for control and data acquisition:

- The testing machine computer and associated controller was used to control the crosshead displacement to match the target moment as a function of the input from the strain gauge placed on the upper metal moment-loading arm (for control).
- The data acquisition computer saved data from the strain gauge placed on the lower metal moment-loading arm (for additional monitoring).
- The image acquisition computer received cyclic data from the testing machine, sent the signal to the camera to take a picture every 50 cycles, and received and saved the picture from the camera.

Crack front location versus number of cycles was extracted from the automated digital image-based tracking method [31,32] at selected number of cycles. There was some noise on the detected delamination front due to the effect of the adhesive, the reinforcement edge, the stitching colouring, etc. Thus, local regression smoothing [50] was used to smooth the detected crack front throughout the specimen width. The local regression smoothing process uses a moving average method, where each smoothed value is determined by neighbouring data points defined within the span. A weighted quadratic polynomial model was used with a span of 20% of the total data points.

The described methodology has two main advantages over the test configuration used in the previously published work [27]. (i) The fatigue test was performed under moment-control, which implies that $\mathcal{G}$ remains constant until the reinforcements affect the flexural modulus of the specimen's arms. Conversely, with displacement-control, the downward trend of $\mathcal{G}$ over time was due to the combined effect of crack length extension and the stiffening effect of the reinforcements. (ii) The translucency of the GFRP material allowed to employ a digital image-based technique for the measurement of the crack front. In comparison with the X-ray radiography used in [27], the digital image-based technique avoided the need for removing the specimen from the text fixture at each measurement (allowing higher sampling frequencies) and the use of contrast liquid that could potentially change the conditions of the delaminating interface.

4. Numerical modelling

4.1. Finite element model implementation in SAMCEF

The model presented in Section 2 was implemented in the Simcenter Samcef 2021.2 software as a new behaviour law. The development was done in a intrusive way in the Samcef solver following the method described in [37]. For the computation of the J-integral, no additional plug-in or API were developed. The J-integral is computed at each integration point of the FEM model. The integration paths are curved lines crossing the cohesive zone formed according to the growth driving direction (GDD). At each integration point of the J-integral, the inter-laminar stress and the displacement jump gradient are computed from the local displacement state of the element at which the integration point belongs to. The J-integral is obtained by numerical integration of all the integration points along the path, using the trapezoidal rule.

In order to improve convergence, a delayed damage strategy that smoothens the transition from the elastic behaviour to damage by applying low viscosity was introduced in the implementation of the method in the Simcenter Samcef 2021.2 software. The artificial viscosity is only applied to the quasi-static damage:

$$\dot{D}^K = \frac{1}{\tau_c}\left(1 - e^{-a_c\langle\omega(\lambda)-D\rangle}\right) \tag{5}$$

where $\omega(\lambda)$ is the static damage function with respect to the equivalent one-dimensional displacement jump without delay effect, a_c is the delay effect coefficient (often equal to 1), and τ_c is the characteristic delay time, which should be set low enough to avoid having an impact on the result and high enough to help convergence.

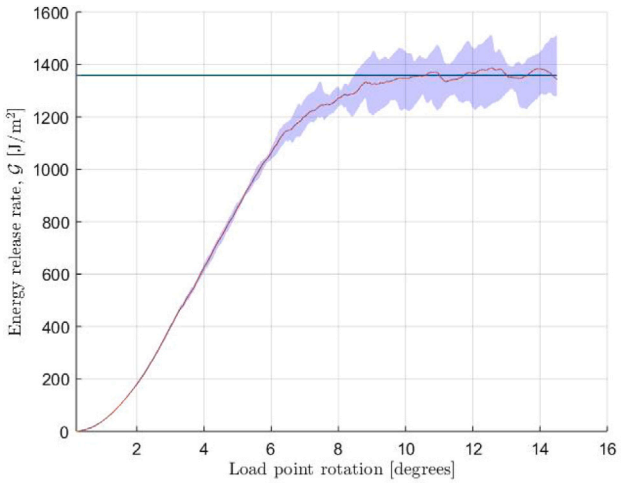

Fig. 6. Averaged, minimum, and maximum curves of mode I energy release rate vs. the load point rotation. The propagation fracture toughness, $\mathcal{G}_{Ic}$, value is represented with a blue solid horizontal line. (For interpretation of the references to colour in this figure legend, the reader is referred to the web version of this article.)

Table 6
Input parameters into the simulation of the demonstrator test.

Input parameters		
$\mathcal{G}_{Ic}$	1.359	N/mm
$\mathcal{G}_{IIc}$	5.4	N/mm
τ_{Io}	20	MPa
τ_{IIo}	40	MPa
η	2	–
K	10^5	N/mm^3
A_I	0.1396	mm/cycle
A_{II}	1	mm/cycle
A_m	1	mm/cycle
p_I	3.753	–
p_{II}	1	–
p_m	1	–

Moreover, a load envelope approach is followed to avoid simulating all fatigue cycles, which would be computationally costly. Thus, the fatigue damage is updated at a certain number of cycles. The damage at a given simulation time is obtained by integration of the damage rate for a given number of cycles. The cycle interval is calculated using a cycle jump algorithm [51] consisting of three steps:

- (1) Compute one fatigue cycle during which the fatigue damage does not evolve.
- (2) The computation of the local cycle jump, ΔN^{loc}, is obtained by dividing the target crack length extension selected by the user, Δa_t, by the local crack growth rate, $\mathrm{d}a/\mathrm{d}N$, at all the integration points in the model (see Eq. (A.24)). A frequency distribution of ΔN^{loc} is calculated from the values obtained at each integration point, and the global cycle jump, ΔN^{glob}, is selected such that a given percentage of integration points is below ΔN^{glob}. This percentage is here set to 5%.
- (3) Update the damage variable at all integration points in all the cohesive elements (see Eq. (A.10)).

4.2. Simulation of the demonstrator test

A validation exercise was performed by comparison of simulation results against the experimental tests (DEM_03 and DEM_04 presented in Section 3.2). For efficiency purposes, only half of the structure was modelled, and symmetry boundary conditions were applied. The structure was modelled by 220 200 hexahedral elements. The cohesive zone was meshed with zero thickness hexahedral cohesive elements sized 0.5 mm x 0.5 mm. The fatigue load sequence applied in the simulation case consists of four steps:

- (1) A quasi-static load ramp from the unloaded state to an applied bending moment of 40 N m.
- (2) A fatigue step with a constant maximum cyclic bending moment of 40 N m until 500,000 cycles.
- (3) A quasi-static load ramp from an applied bending moment of 40 N m to 60 N m.
- (4) A fatigue step with a constant maximum cyclic bending moment of 60 N m until 800,000 cycles.

The elastic ply properties used in the simulation were provided by the company SGRE and are listed in Table 3. Note that the average flexural modulus obtained from three-point bending tests, $E_{11}^f = 37.2$ GPa, was used instead of the longitudinal Young's modulus, $E_{11} = 47.96$ GPa. The input parameters into the inter-laminar damage method are listed in 6. Since it is a pure mode I benchmark test, the introduced shear properties do not have any effect on the produced results. Thus, the fatigue properties that have not been characterized, have been set equal to 1. The mode II fracture toughness, $\mathcal{G}_{IIc}$, and the interfacial tensile strength, τ_{Io}, have been set equal to a representative value for similar materials. The interfacial shear strength, τ_{IIo}, is expressed as [35]:

$$\tau_{IIo} = \tau_{Io}\sqrt{\frac{\mathcal{G}_{IIc}}{\mathcal{G}_{Ic}}} \tag{6}$$

5. Results

5.1. Quasi-static inter-laminar properties

Quasi-static fracture toughness tests were performed following the method specified in Section 3.1.1. The measured mode I energy release versus load point rotation results are shown in Fig. 6. The average, minimum, and maximum curves for the combined data sets are plotted. The propagation fracture toughness, $\mathcal{G}_{Ic}$, obtained by integration of the average curve divided by the span load point rotation in the steady propagation region (plateau) is $\mathcal{G}_{Ic} = 1359$ J/m^2. An initiation $\mathcal{G}$ value of 615 J/m^2 has been estimated from additional quasi-static tests. Details can be found in Appendix D.

5.2. Fatigue inter-laminar properties

Crack growth rate tests under fatigue loading conditions were performed following the method specified in Section 3.1.2. The crack growth rate $\mathrm{d}a/\mathrm{d}N$ is plotted against the energy release rate $\mathcal{G}$ in Fig. 7. The fitting of the combined data set led to a coefficient $A_I = 1.637{\cdot}10^{-13}$ mm/cycle and an exponent $p_I = 3.753$ of Eq. (4).

For the applied $\mathcal{G}$ range in the demonstrator tests presented in Section 5.3 ($130 < \mathcal{G} < 400$ J/m^2), and taking into account that tests were performed at a load ratio $R = 0.1$ and the measured mode I fracture toughness $\mathcal{G}_{Ic} = 1359$ J/m^2 (see Section 5.1), Eq. (A.23) used in the simulation method reads:

$$\frac{\mathrm{d}a}{\mathrm{d}N} = 0.1396\left(\frac{\mathcal{G}(1-0.1^2)}{1359}\right)^{3.753} \tag{7}$$

5.3. Comparison between testing and simulation results of the demonstrator test

The crack front evolution at a selected number of cycles during the tests DEM_02, DEM_03 and DEM_04 are shown in Appendix B, Figs. B.10–B.12, respectively. Note that tests DEM_03 and DEM_04 were designed identical to check the repeatability of the results. It can be observed that both tests show a similar evolution of the crack front in terms of both shape and propagation rate.

Fig. 8 shows the evolution of the delamination front position during fatigue analysis with an applied bending moment of 40 N m (Step 2 of the simulation case presented in Section 4.2). Compared to the experimental results, the simulation results reveal slower crack growth.

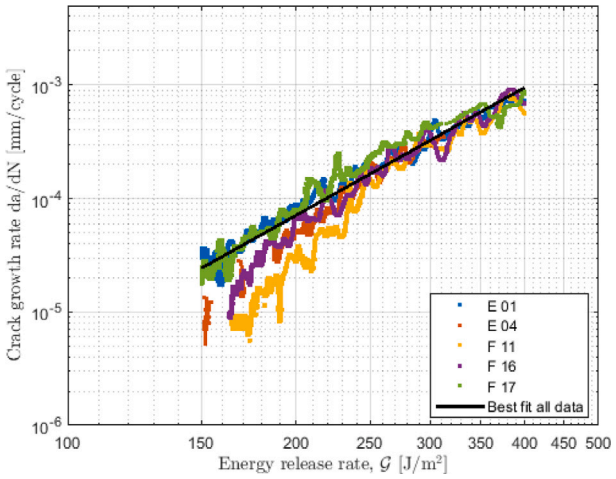

Fig. 7. Crack growth rate vs. energy release rate. Data has been cropped to the applied $\mathcal{G}$ range in the demonstrator tests presented in Section 5.3 and can be found in the open-source online data repository [52].

The maximum difference in crack front position between experimental and simulation results at the different selected number of cycles shown in Fig. 8 (after 50k cycles) is approximately 6.5 mm compared to DEM_04 and 9.3 compared to DEM_03. This difference related to the total crack growth at the same width coordinate is -39% and -48%, respectively. It is worth to mention that the normalization with respect to the total growth at the same with coordinate is inherently imprecise since the front is changing shape and growing in different directions along the crack front, so the points at the same width coordinate are not directly comparable.

At the end of Step 2, the difference between experimental and simulation results is approximately 3 mm (down to +13% of the total crack growth at the same width coordinate). At this point, crack propagation is almost arrested due to the stiffening caused by the reinforcements. When the crack front reaches the reinforcement edges, $\mathcal{G}$ decreases due to the increased combined panel stiffness. This is illustrated with the J-integral contour plots shown in Fig. C.13. According to the Paris' law-like relation (see Eq. (A.23)), the crack growth rate decreases drastically at low values of $\mathcal{G}$. Very low crack growth rates mean that any small difference in load will result in large differences in number of cycles needed to reach the same crack length. Moreover, at low energy release rates, there is a significant variation in the Paris' law-like relation between the different coupon specimens used to characterize the material fatigue properties (see Fig. 7). This could potentially broaden the discrepancy in number of cycles between the experimental results and the numerical prediction.

Fig. 9 shows the evolution of the delamination front position during fatigue analysis with an applied bending moment of 60 N m (Step 4 of the simulation case presented in Section 4.2). Compared to the experimental results, the simulation results reveal slower crack growth. At the end of the analysis (after 670k cycles) the numerical predictions match the DEM_04 experimental test results, while the difference for the DEM_03 experimental test results is less than 5 mm (−8% of the total crack growth at the same width coordinate). In order to get similar crack front propagation, the simulation requires extra 85k load cycles.

The energy release rate, $\mathcal{G}$, was numerically evaluated during the numerical simulations using the J-integral method. The corresponding contour plots during Step 2 and Step 4 (see Section 4.2) are presented in Figs. C.13 and C.14 in Appendix C. Note that before the crack front reaches the reinforced region, the computed J-integral at the mid-width of the specimen remains constant and equal to the analytical value 0.31 N/mm evaluated using Eq. (2), where $M = 40 \cdot 10^3$ N mm is the applied moment in step 1 of the fatigue tests on the demonstrator specimens (from Table 5), $\mu_{12} = 0.308$ is the Poisson's ratio of transverse

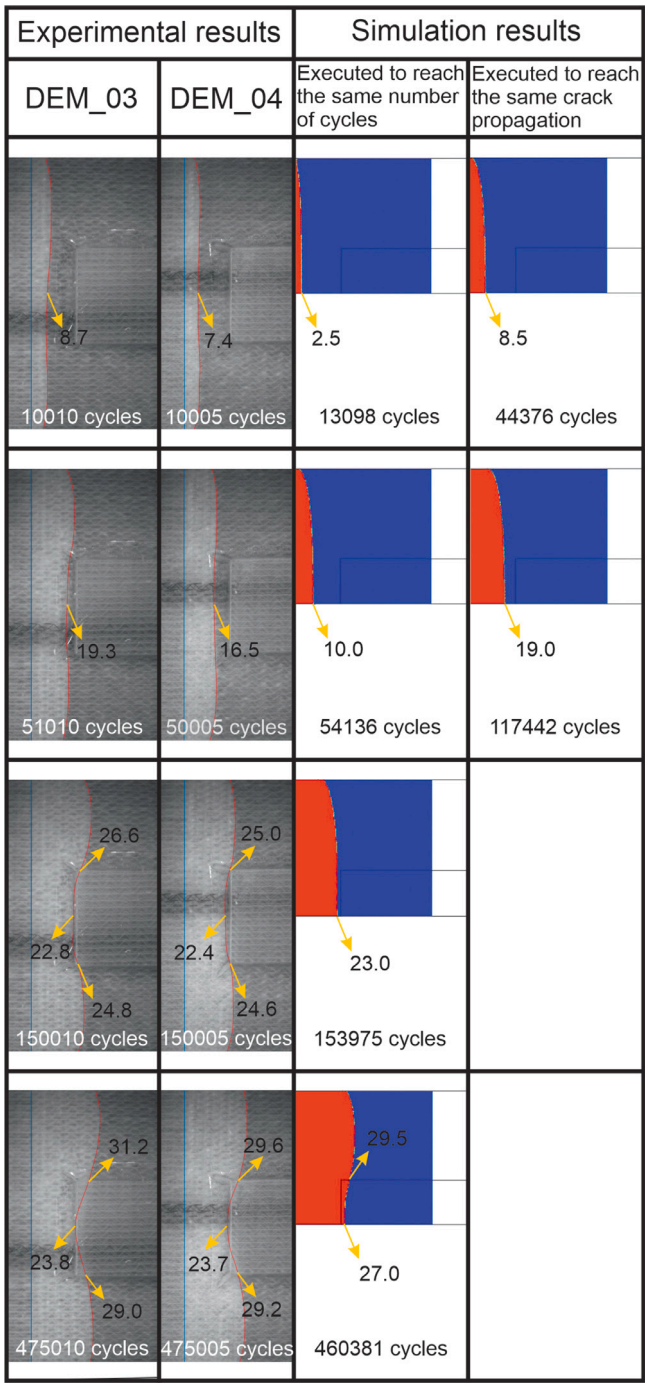

Fig. 8. Comparison of numerical and experimental results for delamination front position (mm) with an applied bending moment of 40 N m (Step 2). The crack extension from the initial pre-crack (blue line) at the middle of the specimen and at the edges of the reinforcements is marked with an arrow. Data of crack extension from the initial pre-crack of all the measured points along the crack front (red line) can be found in [52]. (For interpretation of the references to colour in this figure legend, the reader is referred to the web version of this article.)

extensional strain in the 2-direction to axial extensional strain in the 1-direction (from Table 3), $E_{11}^{f} = 37\,204.06$ MPa is the average flexural modulus obtained from three-point bending tests on coupon specimens (from Table 4), $b = 150$ mm is the design width of the demonstrator specimens (from Fig. 5), and $h = 4.033$ mm is the arm thickness resulting from dividing the average thickness of all specimens in Tables 1 and 2 by the number of plies of the coupon specimens (12 plies) and multiplying by half of the number of plies of the demonstrator specimen (4 plies).

6. Efficiency of the intrinsic implementation of the method in Samcef compared to the extrinsic implementation as a user-defined element in Abaqus

In order to demonstrate the efficiency of the implementation of the fatigue damage law in Samcef, a coupon DCB test under fatigue loading was simulated. The required computational time was compared to that required to run the same simulation case using the implementation of the method as a user-defined element (UEL) in Abaqus. The selection of a simulation case that is limited to a coupon-sized specimen was done because it is simply not feasible to simulate the benchmark case presented in Section 4 with the Abaqus UEL implementation due to the excessive computational cost.

The DCB coupon specimen was modelled using 13,688 hexahedral elements sized 0.3 mm x 0.3 mm x 0.25 mm. The cohesive zone was meshed using 1400 zero-thickness hexahedral cohesive elements sized 0.3 mm x 0.3 mm. The bulk material was isotropic with a Young's modulus of $E = 2.1e6$ MPa and a Poisson's ratio of $\mu = 0.3$. The input parameters related to the fatigue method were: $\mathcal{G}_{Ic} = \mathcal{G}_{IIc} = 1$ N/mm, $\tau_{Io} = \tau_{IIo} = 50$ MPa, $\eta = 2$, $K = 10^5$ N/mm^3, $A_I = A_{II} = A_m = 1$ mm/cycle, and $p_I = p_{II} = p_m = 1$. The fatigue load was applied in two steps:

- (1) A quasi-static load ramp from the unloaded state to an applied bending moment of 1.05 N m.
- (2) A fatigue step with a constant maximum cyclic bending moment of 1.05 N m until 13 mm of crack propagation.

For this particular simulation case, the required simulation time using the implementation of the method as a UEL in Abaqus was 22.5 times greater than the one required using the intrinsic Samcef tool (4.5 h required with the Abaqus implementation, in contrast with 12 min required with the Samcef implementation). It is worth mentioning that most of the computational time required using the extrinsic Abaqus UEL implementation is devoted to the computation of the J-integral and the need for access to global data in the user-defined element in Abaqus, which is achieved through use of the UEXTERNALDB subroutine. For larger models having more cohesive elements and a larger cohesive zone, the computational speed-up with the new implementation in Samcef is ever greater.

7. Summary and conclusions

The inter-laminar damage fatigue method [26] was implemented in the Simcenter Samcef 2021.2 software as a so-called material behaviour law. The advantage compared to other state-of-the-art methods is that it can be applied for prediction of fatigue-driven delamination in 3D structures without the need of adjusting any fitting parameters. Its commercial implementation is readily available and validated on industrial benchmark cases. Moreover, the developed implementation of the method as a built-in tool was shown to be capable to estimate the evolution of interlaminar fatigue damage in a 3D analysis with high efficiency compared to the previous implementation as a user element in Abaqus [26]. The Fortran subroutine for Abaqus was an in-house research code that could only be used for the simulation of FE models with limited numbers of elements due to the use of external files that need to be written and read for the computation of the J-integral at each integration point. The built-in implementation in the Samcef solver requires considerably less computational resources due to the global accessibility of nodal quantities.

In order to assess the prediction capabilities of the method, a demonstrator specimen with varying crack front shape and propagation rate during fatigue loading was used. A full characterization campaign on coupon test specimens was performed to obtain the material properties needed in the model. Then, the demonstrator test was simulated in the Simcenter Samcef 2021.2 software and the results were compared

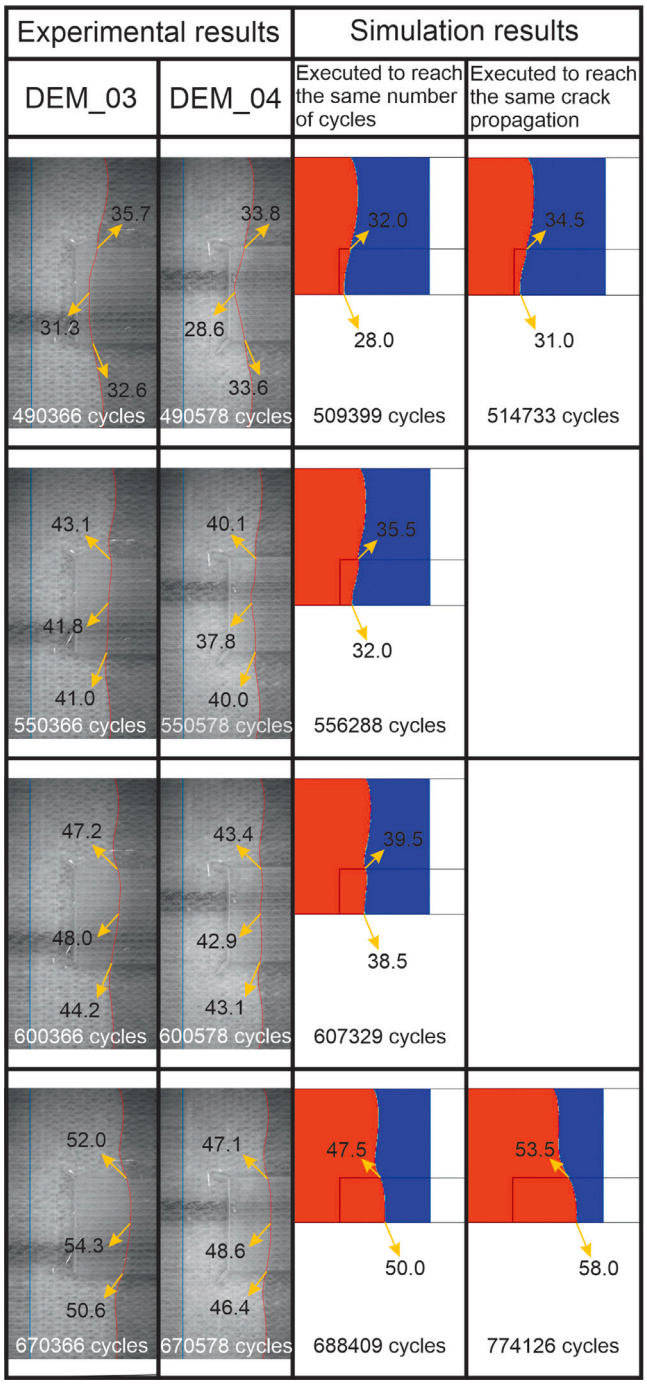

Fig. 9. Comparison of numerical and experimental results for delamination front position (mm) with an applied bending moment of 60 N m (Step 4). The crack extension from the initial pre-crack (blue line) at the middle of the specimen and at the edges of the reinforcements is marked with an arrow. Data of crack extension from the initial pre-crack of all the measured points along the crack front (red line) can be found in [52]. (For interpretation of the references to colour in this figure legend, the reader is referred to the web version of this article.)

to the experimental results. The CPU time was reasonably low (6 h 30 min for a 220 200 elements-model with sequential execution, which might be improved by parallelization on multiple cores).

The shape of the crack front was well reproduced. The crack propagation at the end of the simulation study was underestimated by 8% compared to the experimental results from one demonstrator specimen and coinciding with the results from the other specimen. The difference between experimental and simulation results at the end of the

Table A.7
Algorithm of the fatigue CZM presented in [26].

Input		
$\Delta N\|_{N_n}$, $\mathrm{d}a/\mathrm{d}N\|_{N_n}$, $\{\boldsymbol{\delta}\}$, $D^e\|_{N_n}$, material properties and K		
Output		
$\{\boldsymbol{\tau}\}$, D^e, $[\boldsymbol{C}_\tau]$, ΔN and $\mathrm{d}a/\mathrm{d}N$		
Compute the growth driving direction		
1. Growth driving direction	$-\nabla \frac{\omega_{tot}}{\mathcal{G}_c}$ (see further details in [36])	(A.1)
Compute equivalent one-dimensional cohesive law parameters		
2. Mixed-mode ratio	$B = \frac{\delta_{II}^2}{\delta_I^2+\delta_{II}^2}$	(A.2)
	where $\delta_I = \langle\delta_3\rangle$ and $\delta_{II} = \sqrt{(\delta_1)^2 + (\delta_2)^2}$	(A.3)
3. Equiv. strength	$\mu_o = \sqrt{(\tau_{Io})^2 + \left[(\tau_{IIo})^2 - (\tau_{Io})^2\right] B^\eta}$	(A.4)
4. Equiv. onset displ. jump	$\lambda_o = \frac{\mu_o}{K}$	(A.5)
5. Equiv. fracture toughness	$\mathcal{G}_c = \mathcal{G}_{Ic} + (\mathcal{G}_{IIc} - \mathcal{G}_{Ic})\, B^\eta$	(A.6)
6. Equiv. critical displ. jump	$\lambda_c = \frac{2\mathcal{G}_c}{\mu_o}$	(A.7)
7. Equiv. displ. jump	$\lambda = \sqrt{(\delta_I)^2 + (\delta_{II})^2}$	(A.8)
Compute damage state		
8. Update fatigue damage	$\frac{\mathrm{d}D^e}{\mathrm{d}N} = \left(\frac{\partial D^e}{\partial B}\frac{\partial B}{\partial x_1} + \frac{\partial D^e}{\partial \lambda}\frac{\partial \lambda}{\partial x_1}\right)\frac{\mathrm{d}a}{\mathrm{d}N}$ (see further details in [26])	(A.9)
	$D^e\|_{N_n+\Delta N} = D^e\|_{N_n} + \frac{1}{2}\left(\frac{\mathrm{d}D^e}{\mathrm{d}N}\|_{N_n} + \frac{\mathrm{d}D^e}{\mathrm{d}N}\|_{N_n+\Delta N}\right)\Delta N^{glob}\|_{N_n}$ (see further details in [20])	(A.10)
9. Activation function	$H = \min\left[1, \max\left[0, \frac{\lambda-\lambda_o}{\lambda_c-\lambda_o}\right]\right]$	(A.11)
10. Damage state	$D^e = \max\left[D^e\|_{N_n+\Delta N}, H\right]$	(A.12)
	$D^K = \frac{\lambda_c}{\lambda_D} D^e$	
Compute cohesive tractions		
11. Cohesive tractions	$\{\boldsymbol{\tau}\} = (1 - D^K)K[\boldsymbol{I}][\delta]$	(A.13)
12. Constitutive tangent stiffness $[\boldsymbol{C}_\tau]$ (see further details in [34])		
Establish the cycle jump		
13. Maximum cyclic energy release rate	$J_I = -\sum_k \left[h^k \left(\frac{\sigma_{33}^k \frac{\partial \delta_3^k}{\partial x_1} + \sigma_{33}^{k+1}\frac{\partial \delta_3^{k+1}}{\partial x_1}}{2}\right)\right]$	(A.14)
	$J_{II} = -\sum_k \left[h^k \left(\frac{\sigma_{13}^k \frac{\partial \delta_1^k}{\partial x_1} + \sigma_{13}^{k+1}\frac{\partial \delta_1^{k+1}}{\partial x_1}}{2}\right)\right]$	(A.15)
	$J_{III} = -\sum_k \left[h^k \left(\frac{\sigma_{23}^k \frac{\partial \delta_2^k}{\partial x_1} + \sigma_{23}^{k+1}\frac{\partial \delta_2^{k+1}}{\partial x_1}}{2}\right)\right]$	(A.16)
	where h^k is the integration interval length and k is the number of J-integration points along the entire cohesive zone	
	$\mathcal{G} = J_I + J_{II} + J_{III}$	(A.17)
14. Crack growth rate	$\Phi = \frac{J_{II}+J_{III}}{J_I+J_{II}+J_{III}}$	(A.18)
	$p = \Phi^2 (p_{II} - p_I - p_m) + \Phi p_m + p_I$	(A.19)
	$\log(A) = \Phi^2 \log\left(\frac{A_{II}}{A_m A_I}\right) + \Phi \log(A_m) + \log(A_I)$	(A.20)
	$\mathcal{G}_c = \mathcal{G}_{Ic} + (\mathcal{G}_{IIc} - \mathcal{G}_{Ic})\Phi^\eta$	(A.21)
	$\mathcal{G}_{th} = \mathcal{G}_{IIth} + (\mathcal{G}_{IIIth} - \mathcal{G}_{IIth})\Phi^{\eta_2}$	(A.22)
	$\frac{\mathrm{d}a}{\mathrm{d}N} = A\left(\frac{\mathcal{G}(1-R^2)}{\mathcal{G}_c}\right)^p$ for $\mathcal{G}_{th} < \mathcal{G} < \mathcal{G}_c$	(A.23)
15. Cycle jump	$\Delta N^{loc} = \frac{\Delta a_z}{\left(\frac{\mathrm{d}a}{\mathrm{d}N}\right)}$ (see Section 4 for details on the implementation in the Simcenter Samcef 2021.2 software)	(A.24)

analysis is comparable to the variation in crack propagation among the different demonstrator specimens experimentally tested. Moreover, the experimental tests conducted to obtain input fatigue properties show a great amount of scatter, especially on Paris' law at low values of $\mathcal{G}$, which could be a reason for the difference between the simulated and experimental results in the demonstrator tests.

CRediT authorship contribution statement

L. Carreras: Conceptualization, Methodology, Software, Formal analysis, Investigation, Writing – original draft, Writing – review & editing. **B.L.V. Bak:** Supervision, Conceptualization, Methodology, Software, Data curation, Writing – review & editing, Funding acquisition. **S.M. Jensen:** Methodology, Software, Resources, Writing – review & editing. **C. Lequesne:** Software, Validation, Writing – review & editing. **H. Xiong:** Software, Validation, Visualization. **E. Lindgaard:** Supervision, Conceptualization, Methodology, Software, Data curation, Writing – review & editing, Project administration, Funding acquisition.

Declaration of competing interest

The authors declare that they have no known competing financial interests or personal relationships that could have appeared to influence the work reported in this paper.

Data availability

The data required to reproduce these findings is available to download from doi:10.17632/vbs8kbv9wt.2, an open-source online data repository hosted at Mendeley Data [52].

Acknowledgements

This work was funded by the European Union's Horizon 2020 research and innovation programme under grant agreement No 763990.

Appendix A. Algorithm of the fatigue method

See Table A.7.

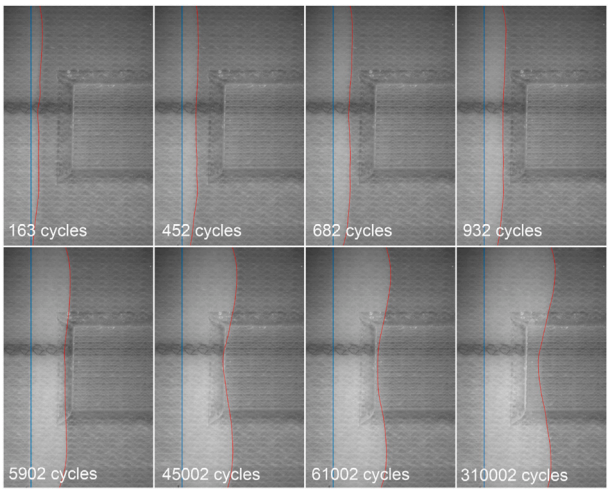

Fig. B.10. Crack front evolution during the test DEM_02. The crack front location is highlighted in red and the blue line corresponds to the initial pre-crack. (For interpretation of the references to colour in this figure legend, the reader is referred to the web version of this article.)

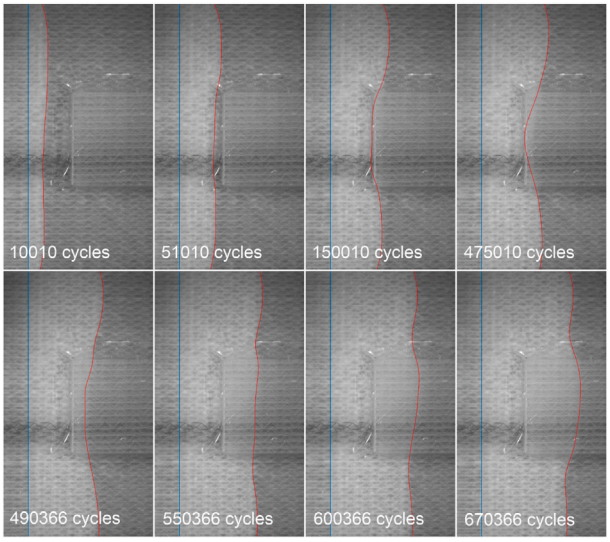

Fig. B.11. Crack front evolution during the test DEM_03. The crack tip location is highlighted in red and the blue line corresponds to the initial pre-crack. (For interpretation of the references to colour in this figure legend, the reader is referred to the web version of this article.)

Appendix B. Crack front evolution during the demonstrator tests

The images shown in Figs. B.10–B.12, as well as the associated raw images and the crack extension data for detected crack fronts are available at open-source online data repository [52].

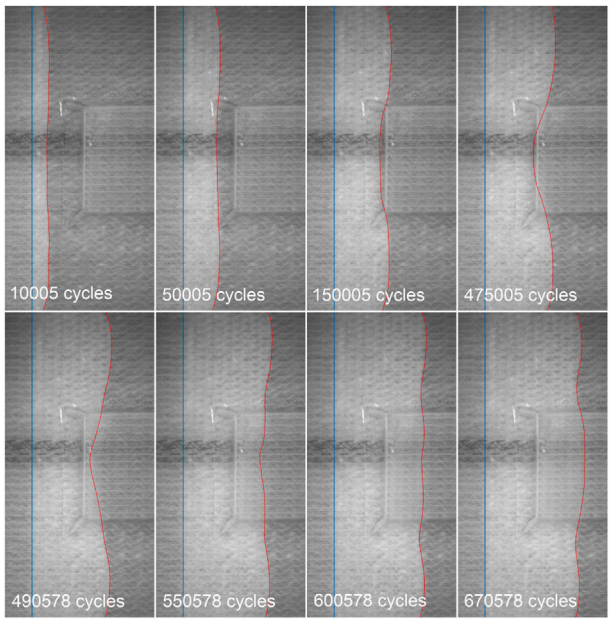

Fig. B.12. Crack front evolution during the test DEM_04. The crack tip location is highlighted in red and the blue line corresponds to the initial pre-crack. (For interpretation of the references to colour in this figure legend, the reader is referred to the web version of this article.)

Appendix C. *J*-Integral evolution during the simulation of the demonstrator test

See Figs. C.13 and C.14.

Appendix D. Additional quasi-static tests

Three additional quasi-static tests (test B in Figs. D.15 and D.16) were conducted to measure and report the initiation $\mathcal{G}$ value, and on request from a reviewer during the peer reviewing process. The additional quasi-static tests were conducted on the compact test fixture as illustrated in Fig. 3. Unlike the quasi-static tests in Fig. 6, the quasi-static tests B made use of a camera setup as illustrated in Fig. 4 to measure the crack front location across the specimen width. The crack length, a, was then computed as the average crack length across the specimen width, as explained previously in Section 3.1.2. Hence, R-curves can be plotted as $\mathcal{G}$ (using Eq. (2)) versus the crack extension $(a - a_0)$. The data is shown below, and the associated (rotation, $\mathcal{G}$)-curves have been compared to the quasi-static tests (tests A) from Fig. 6. The quasi-static tests A and B were conducted on two different test fixtures due to limited availability of test machines, and the tests were performed two years apart due to the paper writing and reviewing process. An initiation $\mathcal{G}$ value of 615 J/m^2 is measured from the additional quasi-static tests (test B). Note that the initiation value of $\mathcal{G}$ is measured from an insert pre-crack which implies certain artificial conditions at the initial crack tip, e.g. a resin pocket that affect the results to an unknown extent. The quasi-static tests B measure a plateau value of $\mathcal{G}$ of 1270 J/m^2. Hence, the initiation value is approximately 50% of the plateau value.

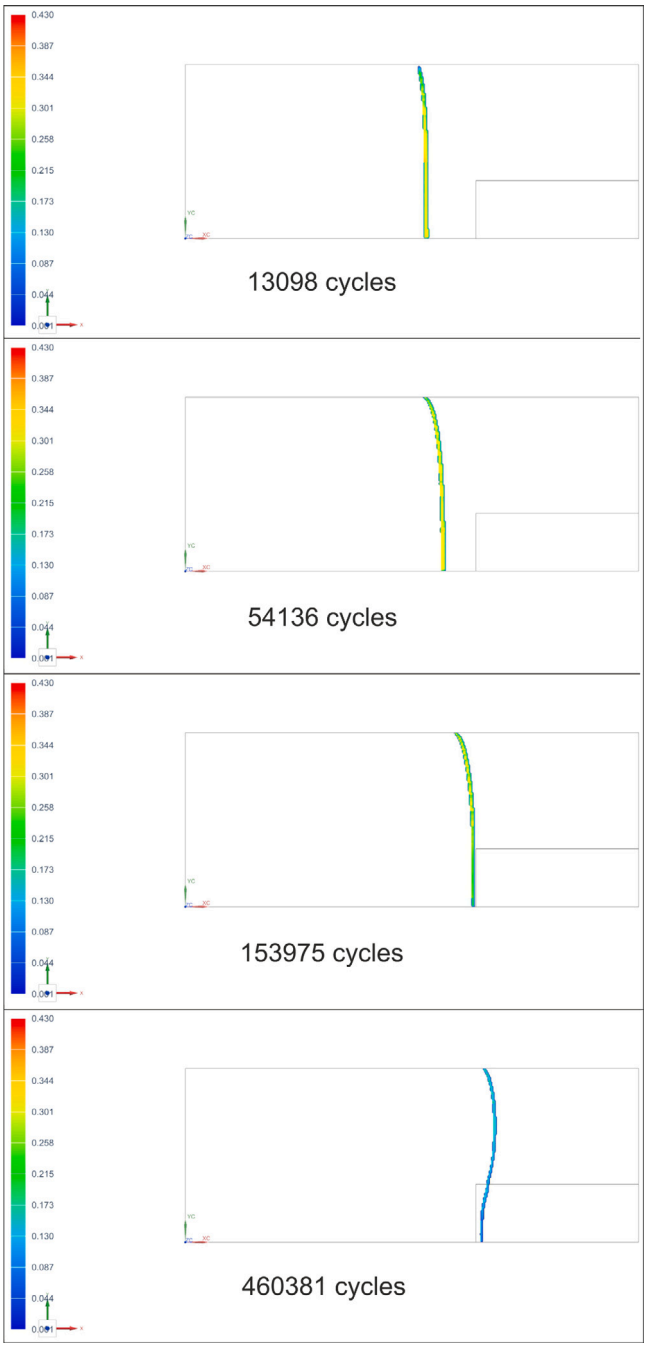

Fig. C.13. Evolution of the mode I-component of the J-integral (N/mm) during Step 2.

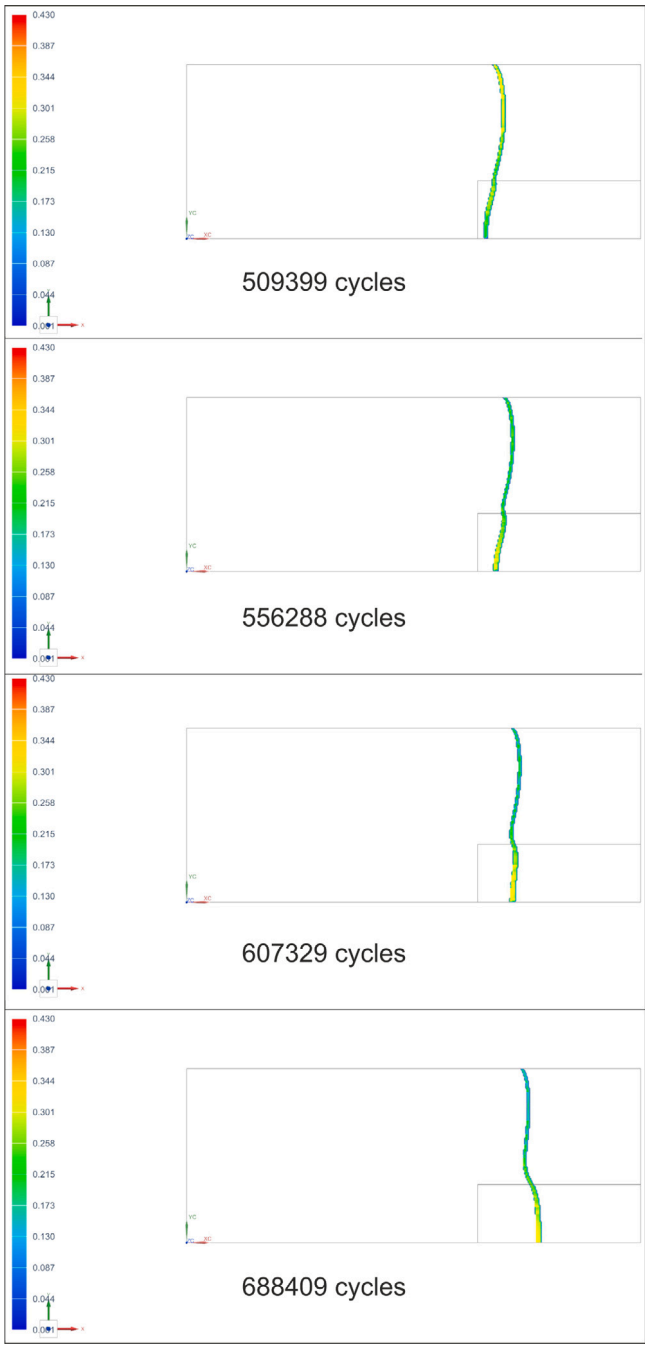

Fig. C.14. Evolution of the mode I-component of the J-integral (N/mm) during Step 4.

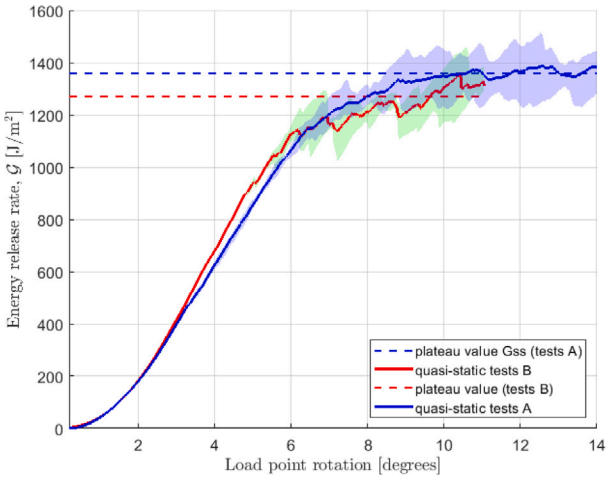

Fig. D.15. Mode I energy release rate vs. the load point rotation in tests A and B.

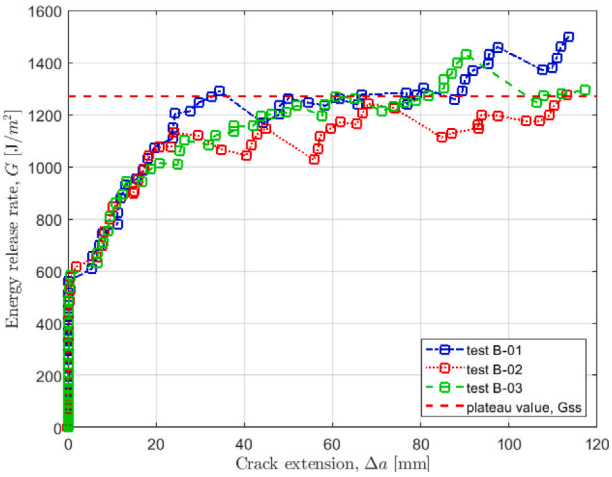

Fig. D.16. Mode I energy release rate vs. the crack length in test B.

References

[1] CMH-17-3G. Composite materials handbook. In: Volume 3: Polymer matrix composites materials useage, design and analysiss. SAE International; 2022.

[2] Bak BLV, Sarrado C, Turon A, Costa J. Delamination under fatigue loads in composite laminates: a review on the observed phenomenology and computational methods. Appl Mech Rev 2014;66(6).

[3] Turon A, Bak BLV, Lindgaard E, Sarrado C, Lund E. Interface elements for fatigue-driven delaminations in advanced composite materials. In: Numerical modelling of failure in advanced composite materials. Elsevier; 2015, p. 73–91.

[4] Ortiz M, Pandolfi A. Finite-deformation irreversible cohesive elements for three-dimensional crack-propagation analysis. Int J Numer Methods Eng I 1999;44:1267–82.

[5] Alfano G, Crisÿeld MA. Finite element interface models for the delamination analysis of laminated composites: mechanical and computational issues. Internat J Numer Methods Engrg 2001;50:1701–36.

[6] Camanho PP, Dávila CG, de Moura MF. Numerical simulation of mixed-mode progressive delamination in composite materials. J Compos Mater 2003;37(16):1415–38.

[7] Goyal VK, Johnson ER, Dávila CG. Irreversible constitutive law for modeling the delamination process using interfacial surface discontinuities. Compos Struct 2004;65:289–305.

[8] Lindgaard E, Bak BLV, Glud JA, Sjølund J, Christensen ET. A user programmed cohesive zone finite element for ansys mechanical. Eng Fract Mech 2017;180:229–39.

[9] Jensen SM, Martos MJ, Bak BLV, Lindgaard E. Formulation of a mixed-mode multilinear cohesive zone law in an interface finite element for modelling delamination with r-curve effects. Compos Struct 2019;216:477–86.

[10] Jensen SM, Martos M, Lindgaard E, Bak BLV. Inverse parameter identification of n-segmented multilinear cohesive laws using parametric finite element modeling. Compos Struct 2019;225:111074.

[11] Trabal GG, Bak BLV, Chen B, Lindgaard E. An adaptive floating node based formulation for the analysis of multiple delaminations under quasi-static loading. Composites A 2022;156:106846.

[12] Trabal GG, Bak BLV, Chen B, Jensen SM, Lindgaard E. Delamination toughening of composite laminates using weakening or toughening interlaminar patches to initiate multiple delaminations: A numerical study. Eng Fract Mech 2022;108730.

[13] ABAQUS/StandArd user's manual, version 6.14. United States: Dassault Systèmes Simulia Corp; 2014.

[14] Robinson P, Galvanetto U, Tumino D, Bellucci G, Violeau D. Numerical simulation of fatigue-driven delamination using interface elements. Internat J Numer Methods Engrg 2005;63(13):1824–48.

[15] Turon A, Costa J, Camanho P, Dávila C. Simulation of delamination in composites under high-cycle fatigue. Composites A 2007;38(11):2270–82.

[16] Pirondi A, Moroni F. A progressive damage model for the prediction of fatigue crack growth in bonded joints. J Adhes 2010;86(5–6):501–21.

[17] Harper PW, Hallett SR. A fatigue degradation law for cohesive interface elements - development and application to composite materials. Int J Fatigue 2010;32:1774–87.

[18] Kawashita LF, Hallett SR. A crack tip tracking algorithm for cohesive interface element analysis of fatigue delamination propagation in composite materials. Int J Solids Struct 2012;49:2898–913.

[19] De Moura M, Gonçalves J. Cohesive zone model for high-cycle fatigue of adhesively bonded joints under mode i loading. Int J Solids Struct 2014;51(5):1123–31.

[20] Bak BLV, Turon A, Lindgaard E, Lund E. A simulation method for high-cycle fatigue-driven delamination using a cohesive zone model. Internat J Numer Methods Engrg 2016;106(3):163–91.

[21] Tao C, Mukhopadhyay S, Zhang B, Kawashita LF, Qiu J, Hallett SR. An improved delamination fatigue cohesive interface model for complex three-dimensional multi-interface cases. Composites A 2018;107:633–46.

[22] Zhang B, Kawashita LF, Hallett SR. Composites fatigue delamination prediction using double load envelopes and twin cohesive models. Composites A 2020;129:105711.

[23] Zhang B, Allegri G, Hallett SR. Embedding artificial neural networks into twin cohesive zone models for composites fatigue delamination prediction under various stress ratios and mode mixities. Int J Solids Struct 2022;236:111311.

[24] Dávila C. From sn to the paris law with a new mixed-mode cohesive fatigue model for delamination in composites. Theor Appl Fract Mech 2020;106:102499.

[25] Trabal GG, Bak BLV, Chen B, Carreras L, Lindgaard E. An adaptive floating node based formulation for the analysis of multiple delaminations under high cycle fatigue loading. Composites A 2022;160:107036.

[26] Carreras L, Turon A, Bak BLV, Lindgaard E, Renart J, de la Escalera FM, Essa Y. A simulation method for fatigue-driven delamination in layered structures involving non-negligible fracture process zones and arbitrarily shaped crack fronts. Composites A 2019;122:107–19.

[27] Carreras L, Renart J, Turon A, Costa J, Bak BLV, Lindgaard E, de la Escalera FM, Essa Y. A benchmark test for validating 3d simulation methods for delamination growth under quasi-static and fatigue loading. Compos Struct 2019;210:932–41.

[28] Bak BLV, Turon A, Lindgaard E, Lund E. A benchmark study of simulation methods for high-cycle fatigue-driven delamination based on cohesive zone models. Compos Struct 2017;164:198–206.

[29] Lindgaard E, Bak BLV. Experimental characterization of delamination in off-axis gfrp laminates during mode i loading. Compos Struct 2019;220:953–60.

[30] Jensen SM, Bak BLV, Bender JJ, Carreras L, Lindgaard E. Transient delamination growth in gfrp laminates with fibre bridging under variable amplitude loading in g-control. Composites B 2021;225:109296.

[31] Bak BLV, Lindgaard E. A method for automated digital image-based tracking of delamination fronts in translucent glass fibre-laminated composite materials. Strain 2020;56(4):e12345.

[32] Jensen SM, Bak BLV, Bender JJ, Lindgaard E. Transition-behaviours in fatigue-driven delamination of gfrp laminates following step changes in block amplitude loading. Int J Fatigue 2021;144:106045.

[33] Simcenter samcef software package, Siemens Digital Industries Software (v2021.2).

[34] Turon A, Camanho PP, Costa J, Dávila C. A damage model for the simulation of delamination in advanced composites under variable-mode loading. Mech Mater 2006;38(11):1072–89.

[35] Turon A, Camanho P, Costa J, Renart J. Accurate simulation of delamination growth under mixed-mode loading using cohesive elements: Definition of interlaminar strengths and elastic stiffness. Compos Struct 2010;92(8):1857–64.

[36] Carreras L, Bak BLV, Turon A, Renart J, Lindgaard E. Point-wise evaluation of the growth driving direction for arbitrarily shaped delamination fronts using cohesive elements. Eur J Mech A Solids 2018;72:464–82.

[37] Carreras L, Lindgaard E, Renart J, Bak BLV, Turon A. An evaluation of mode-decomposed energy release rates for arbitrarily shaped delamination fronts using cohesive elements. Comput Methods Appl Mech Engrg 2019;347:218–37.

[38] Dessureautt M, Spelt J. Observations of fatigue crack initiation and propagation in an epoxy adhesive. Int J Adhes Adhes 1997;17(3):183–95.

[39] Sørensen BF, Jacobsen TK. Large-scale bridging in composites: R-curves and bridging laws. Composites A 1998;29(11):1443–51.
[40] Sørensen BF, Jørgensen K, Jacobsen TK, Østergaard RC. Dcb-specimen loaded with uneven bending moments. Int J Fract 2006;141(1):163–76.
[41] Svenninggaard J, Andreasen J, Bak B, Lindgaard E. Text fixture for double cantilever beam (dcb) specimens subjected to uneven bending moments. In: 16th Internal DCAMM symposium. 2017.
[42] Jensen SM, Carreras L, Lequesne C, Bak BLV, Lindgaard E. A crack growth rate model with load history effects for mode I fatigue-driven delamination under multi-level block loading. 2023, in press.
[43] Hutchinson JW, Suo Z. Mixed mode cracking in layered materials. Adv Appl Mech 1991;29:63–191.
[44] Bao G, Ho S, Suo Z, Fan B. The role of material orthotropy in fracture specimens for composites. Int J Solids Struct 1992;29(9):1105–16.
[45] Hwang W, Han K. Interlaminar fracture behavior and fiber bridging of glass-epoxy composite under mode i static and cyclic loadings. J Compos Mater 1989;23(4):396–430.
[46] Yao L, Alderliesten R, Zhao M, Benedictus R. Bridging effect on mode i fatigue delamination behavior in composite laminates. Composites A 2014;63:103–9.
[47] Donough M, Gunnion A, Orifici A, Wang C. Scaling parameter for fatigue delamination growth in composites under varying load ratios. Compos Sci Technol 2015;120:39–48.
[48] Farmand-Ashtiani E, Cugnoni J, Botsis J. Effects of large scale bridging in load controlled fatigue delamination of unidirectional carbon-epoxy specimens. Compos Sci Technol 2016;137:52–9.
[49] Yao L, Alderliesten R, Benedictus R. The effect of fibre bridging on the paris relation for mode i fatigue delamination growth in composites. Compos Struct 2016;140:125–35.
[50] Mathworks inc. filtering and smoothing data., Available at: https://se.mathworks.com/help/curvefit/smoothing-data.html.
[51] Van Paepegem W. Development and finite element implementation of a damage model for fatigue of fibre-reinforced polymers. GUAP; 2002.
[52] Carreras L, Bak BLV, Jensen SM, Lequesne C, Chiong H, Lindgaard E. Experimental data set from a gfrp experimental benchmark case for validating the simulation of mode i fatigue-driven delamination in composite laminates. Mendeley Data 2022. http://dx.doi.org/10.17632/vbs8kbv9wt.2, v2 (2022).